Journal of CO2 Utilization 68 (2023) 102381

Contents lists available at ScienceDirect

Journal of CO2 Utilization

journal homepage: www.elsevier.com/locate/jcou

CO_2 methanation over Ni-Al LDH-derived catalyst with variable Ni/Al ratio

Yan Resing Dias, Oscar W. Perez-Lopez [*,1]

Laboratory of Catalytic Processes–PROCAT, Department of Chemical Engineering, Federal University of Rio Grande do Sul (UFRGS), Ramiro Barcelos street, 2777, CEP 90035-007 Porto Alegre, RS, Brazil

ARTICLE INFO

Keywords:
CO_2 methanation
H_2 carrier
LDH-derived catalysts
Ni-Al proportion
Basicity

ABSTRACT

CO_2 methanation is a promising technology to recycle CO_2 into useful chemicals, fuels, and energy, avoiding its emissions in the atmosphere, as well as for the purification of H_2 streams containing CO_2. In this work, Ni-Al LDH-derived catalysts with Ni/Al ratio between 0.5 and 4 were prepared by co-precipitation and evaluated in CO_2 methanation. The samples were characterized by N_2 physisorption, X-ray diffraction, temperature-programed reduction, temperature-programmed desorption (CO_2-TPD, H_2-TPD) and oxidation. Catalytic tests were carried out in a fixed-bed reactor at atmospheric pressure, inlet mixture of H_2:CO_2:N_2 = 4:1:15 and GHSV = 60000 mL $(g_{cat}\ h)^{-1}$, in stepwise mode (200–400 °C) and stability at 300 °C. The catalysts presented high activity and selectivity, reaching 92.3 % of CO_2 conversion at 300 °C, along with 100 % CH_4 selectivity for the catalyst with NiAl = 2 due to its high number of weak-to-medium strength basic sites. The amount of H_2-chemisorbed was higher for NiAl = 1, whereas the highest number of basic sites was for NiAl = 2. These results indicate that LDH-derived Ni-Al catalysts with a Ni/Al ratio between 1 and 2 would be suitable for CO_2 methanation.

1. Introduction

Carbon dioxide (CO_2) emission is a rising threat to the global environment, as it is a leading greenhouse gas (GHG) in terms of total volume emitted [1,2]. In 2020, although CO_2 total emissions shared the lowest amount since 2011 given the Covid-19 pandemic outbreak, more than 32 Gton were emitted, showing that mitigating emissions must be a major global concern to achieve a sustainable, decarbonized economy [3]. However, it is an enormous challenge as the majority of energy and fuel consumption globally relies on fossil sources such as oil, coal, and natural gas, representing 83 % of primary energy consumption in 2020 [3].

Many governments, companies, and researchers have been diligently developing and implementing technologies and processes that could allow reduced carbon emissions, either by capturing or even avoiding CO_2 emissions at all [4]. An interesting alternative, which contributes not just to reduce emissions, but also to using captured carbon as an energy and chemical source, is the CO_2 conversion to numerous chemical compounds such as methane (CH_4), methanol (CH_3OH), ethanol (C_2H_5OH), among others. In this context, CO_2 methanation rises as a promising chemical route to CO_2 utilization [5,6].

CH_4 produced by CO_2 hydrogenation may be used as an energy source, fuel, or feedstock to obtain fine chemicals [7,8]. CH_4 is a carrier of H_2 obtained by water splitting using renewable energy sources such as solar and wind, as CH_4 is a more stable, safer-to-work molecule and easier to transport compared to H_2. Then, CH_4 can be directly distributed in existent natural gas grids [9–11]. Moreover, methanation can be applied to CO and CO_2-contaminated H_2 stream purification to use in fuel cells and ammonia synthesis, which demand high-purity H_2 feedstock [12,13].

The general CO_2 methanation reaction involves the hydrogenation of CO_2 producing CH_4 and H_2O (Eq. 1). However, considering the thermodynamic aspects of the process, the reaction occurs in a two-step mechanism, starting with the mildly endothermic reverse water-gas shift (RWGS, Eq. 2) reaction producing CO, which is therefore converted to CO_2 via the highly exothermic CO methanation reaction (Eq. 3) [5,9,14,15]. The high exothermicity of the overall process thermodynamically favors its occurrence in temperatures as low as 200 °C, where theoretically full CO_2 conversion could be attained. However, due to kinetics limitations in low temperatures and difficulty in activating CO_2, highly active and selective catalysts are required to perform this reaction. CO_2 methanation can be easily carried out at atmospheric pressure

* Corresponding author.
E-mail address: perez@ufrgs.br (O.W. Perez-Lopez).
[1] ORCID: 0000-0002-5700-7508.

https://doi.org/10.1016/j.jcou.2022.102381
Received 26 September 2022; Received in revised form 7 December 2022; Accepted 21 December 2022
Available online 26 December 2022

and low temperatures. However, at temperatures higher than 400 °C, RWGS reaction becomes favored, which limits the temperature range from 200 to 450 °C [15–19].

$$4\ H_2 + CO_2 \leftrightarrows CH_4 + 2\ H_2O\ \Delta H_R^0 = -165\ kJ\ mol^{-1} \quad (1)$$

$$H_2 + CO_2 \leftrightarrows CO + H_2O\ \Delta H_R^0 = 41\ kJ\ mol^{-1} \quad (2)$$

$$3\ H_2 + CO \leftrightarrows CH_4 + H_2O\ \Delta H_R^0 = -206\ kJ\ mol^{-1} \quad (3)$$

Although Ni-based supported catalysts are widely used, LDH-derived materials have been recently spotlighted as interesting candidates as catalysts for CO_2 methanation [20–26]. These materials are comprised of multiple positively-charged layers or lamellae of combined divalent (Ni^{2+}, Mg^{2+}, Cu^{2+}, etc.) and trivalent (Al^{3+}, Fe^{3+}, etc.) metal cations surrounded by hydroxide ions, intercalated by anions (CO_3^{2-}, OH^-) that act as compensation charges and H_2O [24]. Such characteristics as variable composition, adjustable acid-base property, high surface area and dispersion, low crystallite size, as well as high stability and adsorption capacity, are highly sought after in materials to use as catalysts [19,24].

Some papers addressed Ni-Al LDH-derived catalysts applied to CO_2 methanation. Abate et al. (2016) investigated the effect of different pH during catalysts preparation, using NaOH and Na_2CO_3 alkaline solution to obtain a pH 12 (Ni-Al 12) and Na_2CO_3 (Ni-Al 8.7) to a pH 8.7 catalysts, with fixed Ni content (75–80 % wt.). Ni-Al 12 exhibited slightly higher CO_2 conversion and CH_4 yield, around 85 % at 300 °C when compared to Ni-Al 8.7 and a commercial catalyst. The higher activity of Ni-Al 12 was attributed to improved reducibility, higher metallic surface area, and dispersion [27]. Daroughegi et al. (2017) studied the effect of ultrasound assistance during co-precipitation, using a NaOH alkaline solution (pH = 10). A 25 % (wt.) Ni catalyst reached 74 % CO_2 conversion at 350 °C, which was due to a higher number of active sites – higher specific surface area and dispersion – and improved reducibility [28].

Gabrovska et al. (2012) prepared catalysts with Ni^{2+}/Al^{3+} (M^{II}/M^{III}) of 0.5, 1.5, and 3. While at low reduction temperatures of 400–450 °C the catalyst with the highest Ni amount showed higher activity, in higher ones (530–600 °C) the catalyst with the lowest Ni amount was more active due to facilitated reduction [29]. Guo et al. (2018) prepared high Ni^{2+}/Al^{3+} ratio (M^{II}/M^{III} = 1–6) catalysts by hydrothermal synthesis, where Ni_5Al-MO (5/1) presented 89.4 % CO_2 conversion and 99 % CH_4 selectivity at 250 °C, attributed to basicity and reducibility properties. However, partially segregated NiO was formed during calcination, presenting a high mean crystallite size (20 nm approx.) upon reduction to Ni^0 [30]. Wierzbicki et al. (2017) synthesized Ni-Mg-Al catalysts, using NaOH alkaline solution (pH = 9.5–10), with fixed M^{II}/M^{III} = 3 and variable Ni/Mg content (0.6–9). The catalyst with higher Ni content (42 % wt.) presented the highest number of basic sites, improved reducibility, and the lowest crystallite size, reaching 72 % CO_2 conversion and 99 % CH_4 selectivity at a low temperature of 250 °C [31].

Previously, our group studied Ni-Al and Co-Al LDH-derived catalysts in CO_2 methanation, finding out that basicity plays a pivotal role in catalytic performance [32]. Thereby, the present work aimed to produce high-purity, co-precipitated Ni-Al LDH-derived mixed oxides, ranging from a wide molar proportion M^{II}/M^{III} = 0.5–4, seeking to evaluate the best ratio to obtain catalysts with features such as small crystallite size, high dispersion, improved reducibility and proper basicity, which can provide high catalytic performance and resistance to deactivation in CO_2 methanation reaction.

2. Experimental

2.1. Catalyst preparation

The precursor salts nickel nitrate ($Ni(NO_3)_2{\cdot}6H_2O$, 97 % P.A.), aluminum nitrate ($Al(NO_3)_20.9\ H_2O$, 98 % P.A.), sodium carbonate (Na_2CO_3, 99.5 % ACS) and sodium hydroxide (NaOH, 97 % ACS) were provided by Synth and used as received. The catalysts were prepared by the co-precipitation method as described in detail in previous papers by our group [32–34]. A nitrate solution (1 M) with required proportions and an alkaline solution (2 M) with Na_2CO_3 and NaOH (50/50 %M) were dropwise-added continuously in a jacketed reactor maintained at 50 °C and constant pH (8 ± 0.1). The precipitate solution was collected and aged for 1 h at 60 °C under vigorous agitation, then washed and filtered until conductivity reached less than 50 μS. The resulting material was dried at 80 °C overnight, sieved (32–42 mesh), and calcined in synthetic air at 600 °C for 6 h to obtain the mixed oxide catalysts. The prepared catalysts, which are summarized in Table 1, were denoted as NixAly, where x and y are the molar proportions of Ni (M^{II}, divalent metal) and Al (M^{III}, trivalent metal), respectively.

Table 1
Molar proportions of co-precipitated LDH catalysts.

Samples	Ni (%M)	Al (%M)	M^{II}/M^{III} molar ratio
Ni33Al66	33	66	0.5
Ni50Al50	50	50	1
Ni66Al33	66	33	2
Ni80Al20	80	20	4

2.2. Catalyst characterization

To obtain the physicochemical properties of calcined samples, N_2 physisorption analyzes were performed via a Quantachrome 4200e pore and surface analyzer. The samples were degassed under vacuum for 3 h at 300 °C, and then analyses were performed with liquid N_2 (−196 °C). Multipoint BET and BJH methods were employed to estimate the specific surface area, and pore volume and size, respectively [35].

X-ray diffractometry (XRD) was performed in a D2 Phaser (Bruker, 30 kV, 10 mA) diffractometer, with Cu-Kα radiation (λ = 0.154 nm) source, to evaluate the crystalline structure. XRD patterns of synthesized material (LDH), fresh samples (calcined and reduced), and spent samples (after catalytic tests) were obtained. The average crystallite sizes were estimated using the Scherrer equation [34].

A multipurpose equipment (SAMP3), equipped with a thermal conductivity detector (TCD), was used to record thermal analyzes of H_2 temperature-programmed reduction (H_2-TPR), CO_2 (CO_2-TPD) and H_2 (H_2-TPD) temperature-programmed desorption. Reduction profiles were obtained through H_2-TPR analysis. The samples (100 mg) were initially pretreated under N_2 flow at 100 °C. The analyzes were then carried out from 100 to 800 °C at 10 °C min^{-1} under a 5 % H_2/N_2 (30 mL min^{-1}) flow [33].

For both CO_2-TPD and H_2-TPD analyses, the samples were firstly reduced at 600 °C for 1 h with 10 % H_2/N_2 (100 mL min^{-1}) flow. CO_2-TPD analysis was used to measure the basic properties of the catalysts. The reduced samples (100 mg) were purged with pure He flow (30 mL min^{-1}) at 100 °C for 30 min, then the He flow was switched to CO_2 (30 mL min^{-1}) to perform adsorption for 30 min and purged again with He as before. The CO_2 desorption step was recorded from 100 to 800 °C at 10 °C min^{-1} under pure He flow [30,32].

H_2-TPD analysis was employed to obtain the H_2 adsorption profile of the catalysts. The reduced samples (200 mg) were purged with a pure N_2 flow (30 mL min^{-1}) for 30 min at ambient temperature, then H_2 adsorption took place with pure H_2 flow (20 mL min^{-1}) for 1 h and purged with N_2 as previously. The H_2 desorption was measured from 50 °C to 800 °C at 10 °C min^{-1} with pure N_2 flow [36,37]. The surface metallic area and metal dispersion were estimated using Eqs. (4) and (5), respectively, as presented by Stangeland et al. [37]:

$$S_{Ni^0}(m^2 g^{-1}) = \frac{Y \times N_A \times F_S}{A} \quad (4)$$

Table 2
Physicochemical properties of Ni-Al catalysts by N_2 physisorption and H_2-TPD.

Samples	M^{II}/M^{III} molar ratio	S_{BET} (m^2 g^{-1})[a]	V_{pore} (cm^3 g^{-1})[b]	D_{pore} (nm)[b]	S^0_{Ni} (m^2 g^{-1})[c]	Dispersion (γ^0_{Ni}) (%)[c]
Ni33Al66	0.5	295.1	0.374	3.9	15.8	4.6
Ni50Al50	1	216.0	0.284	3.9	23.0	5.0
Ni66Al33	2	175.1	0.332	3.9	17.2	3.2
Ni80Al20	4	139.2	0.321	6.4	8.4	1.4

[a] Obtained via BET method from N_2 physisorption data.
[b] Obtained via BJH method from N_2 physisorption data.
[c] Obtained via H_2-TPD chemisorption data.

$$\gamma_{Ni^0}(\%) = \frac{Y \times F_S}{\frac{W_m}{M_m}} \times 10 \quad (5)$$

where Y represents the amount of chemisorbed H_2 (mol g_{cat}^{-1}), N_A is Avogadro number (6.023×10^{23} atoms mol^{-1}), A is surface Ni atoms located at a unit area (1.54×10^{19} atoms m^{-2}), F_S is the stoichiometric factor ($H_2/Ni = 2$), W_m is Ni metal loading (g_{Ni} g_{cat}^{-1}) and M_m is Ni molar mass (58.69 g_{Ni} mol^{-1}).

Temperature-programmed oxidation (TPO) was employed to evaluate carbon deposits of catalysts spent in stability tests. SDT Q600 thermobalance (TA Instruments) was used, where samples (10 mg) were heated at 10 °C min^{-1} from ambient temperature to 800 °C with synthetic air flow (100 mL min^{-1}) [38].

2.3. Catalytic tests

The catalytic tests were performed as described in the previous papers [32,39,40], utilizing a fixed-bed tubular quartz reactor, heated by an electric resistive furnace and gas flows controlled by digital mass controllers (Sierra Instruments). The gas mixture products were analyzed online in a Varian 3600 Cx gas chromatograph equipped with a thermal conductivity detector and a Porapak-Q column, using N_2 as carrier gas.

The catalyst samples (100 mg) were reduced in situ at 600 °C for 1 h using 100 mL min^{-1} of 10 % H_2/N_2. Activity tests were performed with mixture of H_2:CO_2:N_2 = 4:1:15 (v/v, 100 mL min^{-1}), a GHSV of 60000 mL (g_{cat} h)$^{-1}$ and atmospheric pressure. Variable temperature tests were carried out in stepwise mode from 200 to 400 °C (ΔT = 50 °C) with five GC analyses at each temperature. Stability tests at a fixed temperature of 300 °C were carried out for 300 min (5 h) where GC analyzes were conducted every 10 min

The CO_2 conversion, CH_4 selectivity, and CH_4 yield (on a dry basis) were obtained from Eqs. (6)–(8), respectively:

$$X_{CO_2}(\%) = \frac{F_{CO_2\,in} - F_{CO_2\,out}}{F_{CO_2\,in}} \times 100 \quad (6)$$

$$S_{CH_4}(\%) = \frac{F_{CH_4\,out}}{F_{CH_4\,out} + F_{CO\,out}} \times 100 \quad (7)$$

$$Y_{CH_4}(\%) = X_{CO_2} . S_{CH_4} \times 100 \quad (8)$$

3. Results and discussion

3.1. Catalyst characterization

Table 2 summarizes the specific surface area, pore volume, and average pore diameter estimated from N_2 physisorption analysis of calcined samples (mixed oxides), while Fig. 1 presents the N_2 physisorption isotherms and Fig. S1 (supplementary material) presents the pore volume distributions. The surface area notably decreases when increasing Ni loading, from 295.1 for Ni33Al66 to 139.2 m^2 g^{-1} for Ni80Al20, perhaps due to the increase of Ni loading causing pore blockage, as well as the simultaneous decrease of Al loading, as Al-based oxides present high surface areas [35,41,42]. Pore volume follows the same behavior as surface area, except for Ni50Al50, which had the lowest one. The mean pore diameter was the same for samples until $M^{II}/M^{III} = 2$, with Ni80Al20 presenting the higher one. These results

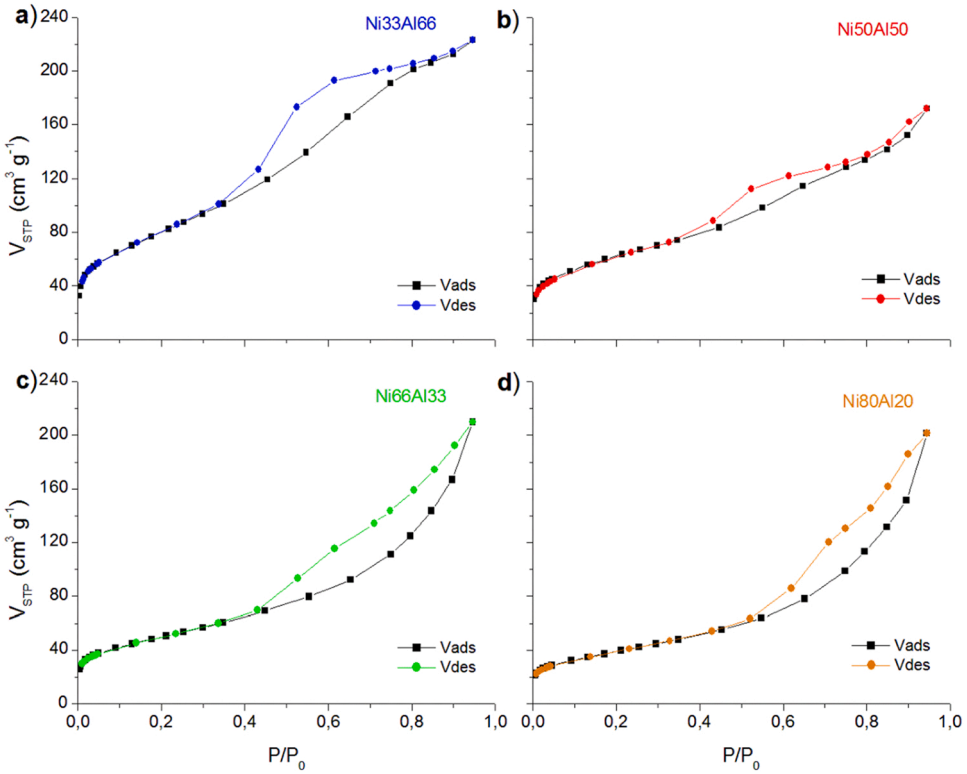

Fig. 1. N_2 physisorption isotherms of Ni-Al calcined catalysts, where: (a) Ni33Al66, (b) Ni50Al50, (c) Ni66Al33, and (d) Ni80Al20.

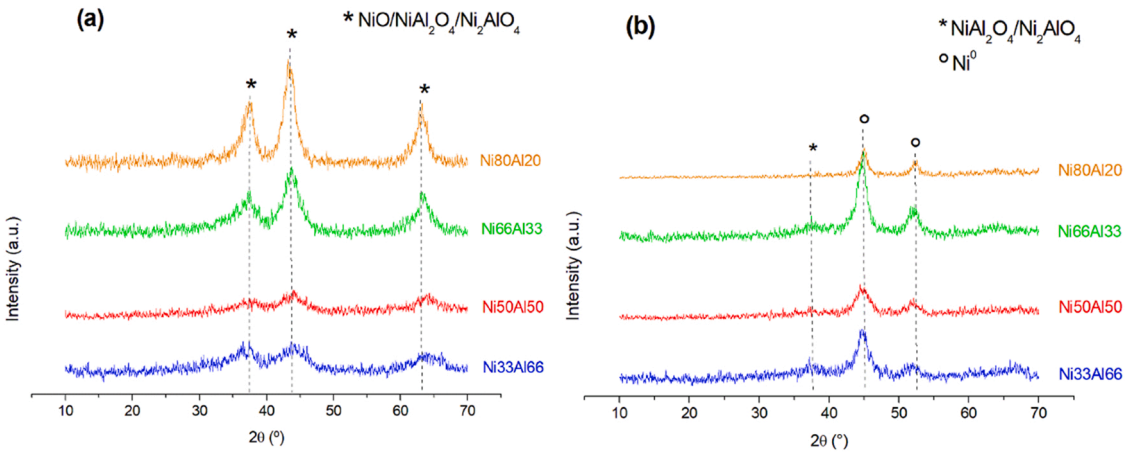

Fig. 2. XRD patterns of (a) calcined and (b) reduced Ni-Al samples.

Table 3
Average crystallite size of fresh reduced (before reaction) and spent (after reaction) samples.

Samples	M^{II}/M^{III} molar ratio	Average crystallite size (nm)		
		D^{a}_{red}	$D^{a,b}_{step}$	$D^{a,c}_{stab}$
Ni33Al66	0.5	3.3	4.1	3.1
Ni50Al50	1	3.3	3.0	3.6
Ni66Al33	2	5.9	4.3	5.8
Ni80Al20	4	6.3	6.8	7.4

[a]Determined from XRD pattern of Ni^0 at 44.8°.
[b]After tests in stepwise mode between 200 and 400 °C.
[c]After 5 h stability tests at 300 °C.

suggest that lower M^{II}/M^{III} proportions improve metal dispersion on the surface, thus enhancing the catalysts textural properties [31]. It should be noted that the decrease in the M^{II}/M^{III} ratio implies a decrease in the amount of Ni and a simultaneous increase of Al in the sample. Considering that Al plays the role of structural promoter, the decrease in the M^{II}/M^{III} ratio results in a catalyst with a higher specific surface area and, as the amount of Ni decreases, the active metal dispersion increases.

The samples present isotherms type IV (a), which indicates capillary condensation followed by hysteresis between adsorption-desorption curves due to the presence of pores with a diameter higher than 4 nm and are characteristic of mesoporous materials (2–50 nm). The samples Ni33Al66 and Ni50Al50 presented hysteresis loop type H2 (b), which may indicate pore blocking in narrow pore necks, meanwhile samples Ni66Al33 and Ni80Al20 have H3 hysteresis that is related to plate-like particles, as found in LDH and LDH-derived materials [43].

The XRD patterns of as-prepared samples (Fig. S2) presented characteristic hydrotalcite peaks (2θ = 11.5°, 23.4°, 35°, 39.8°, 46.7°, 61.8°), demonstrating that LDH-like materials were successfully obtained [31]. XRD patterns of calcined and reduced samples are shown in Fig. 2. The calcined samples presented three main peaks, at 2θ = 37.5°, 43.3°, and 63°. These peaks are ascribed to the NiO phase obtained upon calcination, although may also represent Ni-Al-O spinel phases ($NiAl_2O_4$ - normal, Ni_2AlO_4 - inverse), which are expected for ex-LDH materials; however, cannot be precisely observed through XRD analysis due to similar reflection angles [23,31]. The reduced samples presented main reflections at 44.8° and 52.3° attributed to Ni^0 phase. The peak at 37.5° may be related to Ni-Al-O spinels, mainly for lower M^{II}/M^{III} ratio samples, indicating that the mixed oxides were not completely reduced [23,44]. All reduced samples presented small crystallite sizes, as seen in Table 3, although they show an increase in crystallite size for M^{II}/M^{III} ratios above 1.

Fig. 3 shows the reduction profiles of calcined samples. The samples presented a broad main peak at high temperatures (> 400 °C)

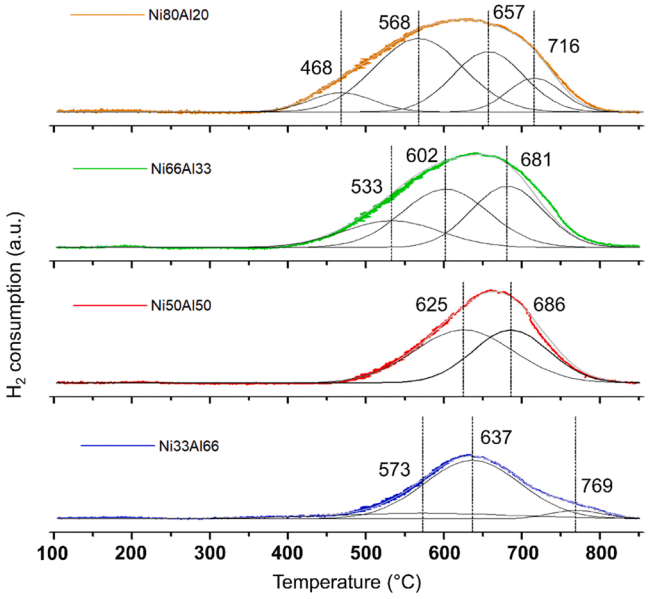

Fig. 3. H_2-TPR profiles of calcined Ni-Al samples.

Table 4
Quantified data from thermal characterization (TPR, TPD, and TPO) of Ni-Al catalysts.

Samples	M^{II}/M^{III} molar ratio	H_2 consumption (μmol g_{cat}^{-1})[a]	CO_2 desorption (μmol g_{cat}^{-1})[b]	H_2 desorption (μmol g_{cat}^{-1})[c]	Carbon deposited (g g_{cat}^{-1})[d]
Ni33Al66	0.5	90.5	11.5	41.0	30.6
Ni50Al50	1	119.7	20.3	59.6	24.1
Ni66Al33	2	154.5	27.3	44.4	22.4
Ni80Al20	4	178.1	21.2	23.2	14.7

[a] Obtained through H_2-TPR profiles.
[b] Obtained through CO_2-TPD profiles.
[c] Obtained through H_2-TPD profiles.
[d] Obtained through TPO profiles.

representing Ni-Al-O spinel mixed oxides reduction to Ni^0. This peak increases for higher M^{II}/M^{III} ratios as well as total H_2 consumption (Table 4), as the Ni content increases [26,30,45]. Bulk NiO reduction, which occurs at lower temperatures, is negligible in these samples, demonstrating that all Ni was in the mixed oxide phase. Reduction of Ni-Al-O oxides is more difficult than of bulk NiO, as the mixed oxides

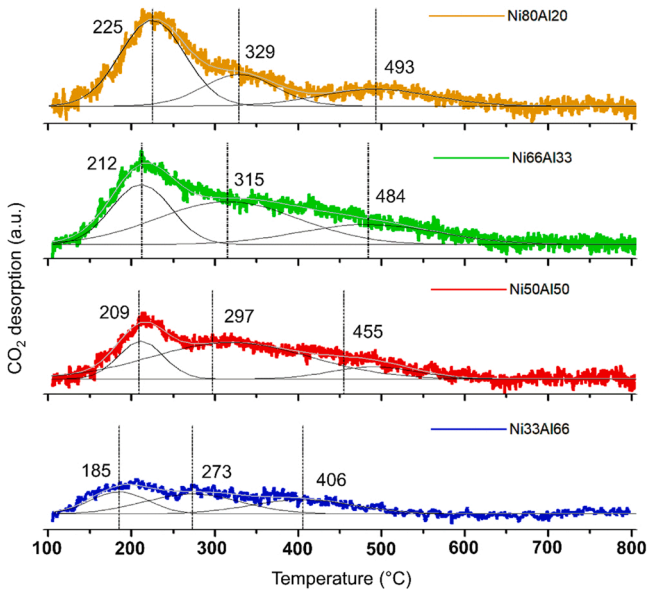

Fig. 4. CO_2-TPD profiles of reduced Ni-Al samples.

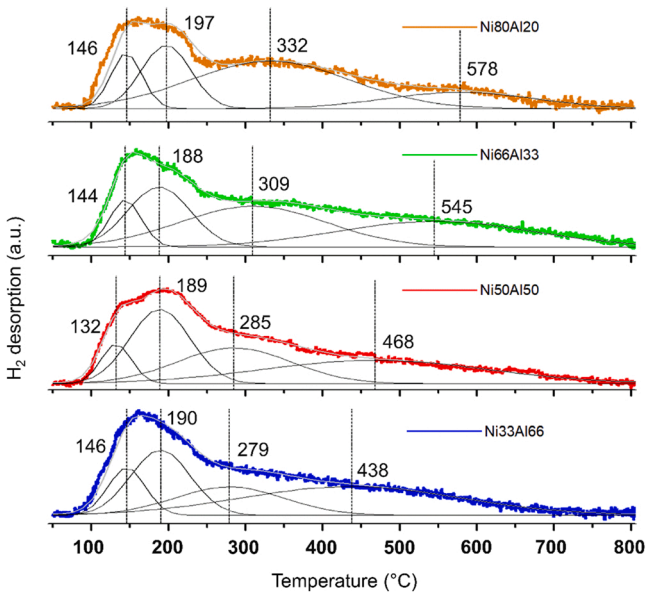

Fig. 5. H_2-TPD profiles of reduced Ni-Al samples (scales amplified compared to Ni50Al50: Ni33Al66 and Ni66Al33 1.5x, Ni80Al20 2.5x).

have strong interaction between Ni^{2+} and Al^{3+} ions and high dispersion of Ni in the lattice [45]. The reduction temperatures were shifted to higher ones when decreasing M^{II}/M^{III} ratio due to a lower amount of Ni-rich phases, where the Ni particles were smaller and consequently have strong interaction with Al [31]. As the peak is considerably broad in all samples, it should be a result of overlapping individual peaks, and then the profiles were refined through deconvolution. This treatment revealed the presence of two to four peaks overlapped, depending on the sample composition. The correspondent reduction temperatures and percentual peak areas are presented in Table S1. The sample with $M^{II}/M^{III} = 1$ (Ni50Al50) presented two peaks, centered at 625 and 686 °C, which can be assigned to Ni_2AlO_4 and $NiAl_2O_4$ spinel reduction, respectively, with similar peak areas. The sample with $M^{II}/M^{III} = 2$ (Ni66Al33) had three peaks, where the Ni_2AlO_4 inverse spinel at 602 °C and the $NiAl_2O_4$ normal spinel at 681 °C. The first peak at 533 °C may be associated with large NiO particles interacting weakly with Ni-Al-O phases, which is then of easier reducibility than spinels [27]. A similar pattern was observed for the sample with $M^{II}/M^{III} = 4$ (Ni80Al20), with the first peak at 468 °C of NiO/Ni-Al-O reduction, a second peak at 568 °C for Ni_2AlO_4, and the third peak at 657 °C for $NiAl_2O_4$. This sample also presented the fourth peak at 716 °C, possibly related to small Ni particles, interacting strongly with Ni-Al-O spinels and/or Al_2O_3 which are hardly reducible.

The sample with a lower M^{II}/M^{III} ratio of 0.5 (Ni33Al66) had a different behavior compared to the other samples. The small first peak at 573 °C could be related to large Ni particles interaction weakly with Ni-Al-O, similarly to Ni66Al33 and Ni80Al20 samples, as it is unlikely that Ni_2AlO_4 spinel was formed given the low Ni content. Then, the sample is mainly formed by $NiAl_2O_4$ spinel, correspondent to the peak at 637 °C, and a small shoulder at 769 °C, which is related to small Ni particles interacting strongly with $NiAl_2O_4$, similarly to Ni80Al20 catalyst. Except for catalyst Ni33Al66, higher M^{II}/M^{III} ratios lead to lower reduction temperatures, for both the first peak (Ni66Al33 and Ni80Al20 only) and spinel-like peaks, which shows its facilitated reduction. Daroughegi et al. (2017) stated that to lower Ni loadings the peak temperatures shift to higher ones whereas the peak intensities decline, revealing a high interaction between catalysts components associated with small Ni crystallite size, which agrees with XRD calculations [28].

The CO_2-TPD profiles of reduced samples are depicted in Fig. 4. The samples presented three peaks, observed through deconvolution, where the peaks ranging from 100 to 250 °C are related to weak basic sites, from 250 to 400 °C to medium basic sites, and from 400 °C onwards to strong basic sites [31,46,47]. All samples show a pronounced peak of weak basicity. The samples with M^{II}/M^{III} from 0.5 to 2 have mainly medium basic sites, while the sample with M^{II}/M^{III} of 4 has more sites of weak basicity. When increasing M^{II}/M^{III} ratio from 0.5 to 2, the proportion of medium basic sites is increased, whereas strong basic sites are less pronounced, as shown in Table S2. The peak temperature for each range increases for higher M^{II}/M^{III} ratios, indicating that basic strength also increases for the higher Ni loadings [31,48]. However, while the basic sites number increases mainly as weak sites for high M^{II}/M^{III} ratios, the catalyst Ni66Al33 has a higher number of medium basic sites, and a total number of weak-to-medium ones, than the other catalysts. This catalyst exhibited the highest total number of basic sites and consequently higher basicity among all catalysts, as shown in Table 4. The presence of high basicity benefits the CO_2 adsorption during the reaction, as it is a mild acidic molecule, facilitating CO_2 activation and thus reaction at the surface. Meanwhile, there is no consensus in the literature on which type of basic sites – weak, medium or strong – are better for CO_2 methanation. Some authors suggest that strong basic sites are responsible to promote activity, while others state these sites adsorbs CO_2 irreversibly and do not participate in the reaction [44,47,49]. The most accepted is that medium basic sites are more prone to promote CO_2 adsorption-dissociation-reaction cycle, as observed in recent studies [44,47,50]. However, regarding weak basic sites, it could also promote CO_2 activation according to some reports [51,52]. Therefore, the Ni66Al33 catalyst presents the best basic properties, as it has mainly weak-to-medium basicity associated with a high density of basic sites.

The H_2-TPD analyses were conducted to evaluate the chemisorption capacity of the samples. As shown in Fig. 5, the profiles had similar trends, where two main regions are observed; the peak ranging from 100 to 250 °C can be related to hydrogen adsorbed on Ni active sites, whereas above 200 °C, the broad peak is attributed to hydrogen highly-interacting with Ni-Al species. However, H_2-spillover species adsorbed at the surface could be also expected at higher temperatures [47,53]. H_2-spillover species comprise H-atoms originated from H_2 dissociated over active sites which migrated from Ni to mixed oxides with high interaction [54–56]. As observed before, each region is comprised of some minor peaks, indicating sites with different metal-hydrogen interactions and small-size particles. Through deconvolution two peaks were obtained at each region, as seen in Table S3, where main H_2 desorption occurs in the second region [53,57]. While the temperature and area of the first and second peaks do not follow a clear trend,

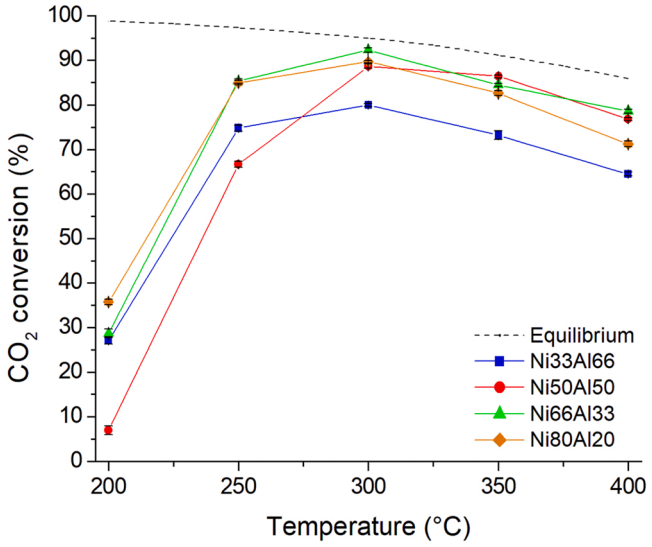

Fig. 6. CO_2 conversion over Ni-Al samples as a function of reaction temperature. Sources of equilibrium curve: Gao et al. (2012), Schaaf et al. (2014).

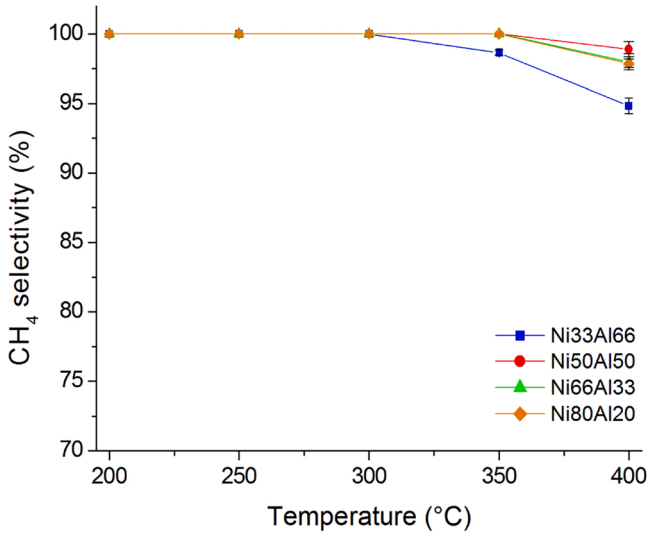

Fig. 7. CH_4 selectivity as a function of reaction temperature for CO_2 methanation over Ni-Al catalysts.

increasing the M^{II}/M^{III} ratio increases the temperature of the third and fourth peaks, also increasing the area of the third peak and decreasing the area of the fourth peak, showing that Ni-Al interaction plays an important role in H_2 adsorption strength, even if adsorption over active sites (Ni^0) is more important to adsorb and activate H_2 [53]. Total H_2 desorption data (Table 4) obtained via H_2-TPD profile integration were used to estimate total surface metallic area (S^0_{Ni}) and dispersion (γ^0_{Ni}) and these results are summarized in Table 2. Both metallic area and dispersion increase when increasing M^{II}/M^{III} ratio until 1 and then decrease for higher M^{II}/M^{III} ratios, and even if Ni66Al33 has a slightly larger metallic area than Ni33Al66 it has lower dispersion due to a higher Ni amount. These results suggest that higher metal dispersion could be attained until equimolar Ni-Al composition by enhancing metal species interaction, whereas further increasing Ni content leads to worse species distribution possibly due to the formation of Ni agglomerates, which agrees with the crystallite sizes estimated through XRD [53].

3.2. Catalytic tests

The catalytic tests were performed firstly in stepwise mode, from 200 °C to 400 °C, where the activity results are expressed in terms of CO_2 conversion as shown in Fig. 6, where the equilibrium curve based on data by Gao et al. (2012) and Schaaf et al. (2014) was also included for reference [58,59]. The conversion had similar trends overall. From 200 to 300 °C, the catalysts with higher Ni content showed higher activity, although all presented a strong increment from 200 to 250 °C, followed by a slight increase at 300 °C, reaching the maximum CO_2 conversion of 92.3 % for Ni66Al33. Although thermodynamics indicates even higher conversions could be attained at low temperatures, these results show that kinetics favors the reaction when increasing temperature; thus, kinetics acts as a limiting factor under 300 °C [15]. Moreover, at 300 °C the CO_2 conversion is near the equilibrium conversion, i.e., close to the maximum feasible conversion. Further increasing to 350 and 400 °C led to the lower catalytic activity of all catalysts, decreasing conversion by around 10–20 %, an effect attributed to reverse water-gas shift (RWGS) reaction being favored at higher temperatures, also increasing H_2O and decreasing CH_4 production [25,30]. Despite having the lowest activity at 200–250 °C among the catalysts, the Ni50Al50 catalyst exhibited a high conversion after 300 °C, like Ni66Al33. This behavior is related to a slower activation of Ni50Al50 due to the strong interaction of mixed oxides, since highly dispersed and small-sized particles are hardly reducible, as observed through XRD and H_2-TPR analysis [28,47]. Therefore, the high metallic area and dispersion of Ni50Al50, associated with its small crystallite size, are responsible for both the low activity at low temperatures and the high activity after 300 °C.

Regarding selectivity, only CH_4 was produced and no CO was detected from 200° to 350°C for all catalysts, as shown in Fig. 7 and Fig. S3, respectively, except for Ni33Al66 which produced less than 2 % CO at 350 °C. At 400 °C, CO was formed for all catalysts at a low amount (< 5 %). Only Ni33Al66 showed more significant CO selectivity, although just around 5 %. As observed at 350–400 °C in CO_2 conversion, CO formation occurs due to the RWGS reaction which is favored at higher temperatures, also leading to increased H_2O formation, which is a product of both CO_2 methanation and RWGS reactions, as stated in the previous literature [30,60,61].

The high activity and selectivity of these catalysts could be assigned mainly to high basicity and small crystallite sizes, although their good dispersion and metallic area may also contribute to their performance, while the specific surface area does not seem relevant [44,62]. Nonetheless, basicity seems to be responsible for the differences in catalytic performance among the samples. The catalyst Ni66Al33 stands out possibly as a consequence of the higher number of basic sites, mainly in the weak-to-medium basicity range, which was observed in previous studies, emphasizing the role of basicity in CO_2 adsorption and activation [30,32]. A similar outcome was reported by Wierzbicki et al. (2016) for Ni-Mg-Al La-doped, LDH-derived catalysts acknowledging that presence of medium-strength basic sites was responsible for high CO_2 adsorption and activity of catalysts towards methanation [50]. Although the reducibility of these samples can be harder to attain than bulk or supported catalysts, it was successfully activated to reach high catalytic performances alongside the aforementioned properties. Therefore, due to the smaller reducible area in the TPR and a higher amount of $NiAl_2O_4$ spinel phase in Ni33Al66, this catalyst presented the lowest activity, because this phase is more difficult to reduce, and even some authors consider it inactive for CO_2 methanation [28]. According to CH_4 yield (Fig. S4), the order of activity at 300 °C (maximum CO_2 conversion and 100 % CH_4 selectivity) is Ni66Al33 > Ni80Al20 ≈ Ni50Al50 > Ni33Al66.

The results clearly show that the role of aluminum is only as a structural promoter, since although the specific surface area increases with the aluminum content in the catalyst, the activity was independent of the specific surface area. This behavior has been verified previously for LDH-derived catalysts [64,65].

The stability of CO_2 conversion and CH_4 selectivity over time-on-stream were evaluated at 300 °C for all catalysts, as shown in Fig. 8, as well as CH_4 and CO yield shown in Fig. S5. All catalysts presented

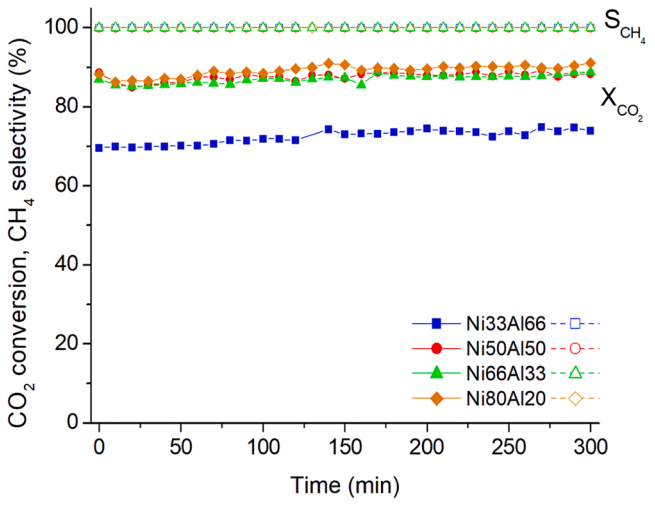

Fig. 8. CO_2 conversion (X_{CO2}) and CH_4 selectivity (S_{CH4}) with the time on stream at 300 °C for CO_2 methanation over Ni-Al catalysts.

high stability, maintaining CO_2 conversion at around 90 % for catalysts with $M^{II}/M^{III} \geq 1$, while for Ni33Al66 ($M^{II}/M^{III} = 0.5$) was around 70 %. CH_4 selectivity was maintained at 100 % for all catalysts during the time-on-stream. These results also indicate that carbon formation and sintering were not significant [30,31].

3.3. Catalyst characterization after reactions

The XRD patterns of spent catalysts are shown in Fig. 9 for both stepwise (a) and stability (b) tests. The samples presented the same peaks as fresh reduced, at 44.8° and 52.3° attributed to Ni^0, showing that the catalysts maintained their active phase after use, along with a peak at 37.5° assigned to unreduced Ni-Al-O spinels, which remained even after reduction and exposed to the reactional environment [23,44]. Regarding the tests in stepwise mode, the spent ones had slight crystallite size differences in comparison to fresh reduced samples (Table 3), where Ni33Al66 and Ni80Al20 showed a small increase. For the stability tests, spent samples did not show appreciable differences in crystallite size in comparison to fresh reduced ones, where only Ni80Al20 had a crystallite size growth. However, the differences in crystallite size were negligible for both stepwise and stability spent samples concerning fresh reduced samples and all catalysts maintained small crystallite size, which indicates that sintering was negligible, and no carbon-related peaks were detected, in agreement with stability tests results.

The TPO profiles of spent catalysts in stability tests are presented in Fig. 10. The catalysts had similar trends with three main regions according to the oxidation temperature. The first region (I) ranging from room temperature to 250 °C shows a weight loss related to moisture adsorbed in the surface and pores and it is verified that the weight loss was proportional to the specific surface area of the samples; the second region (II) ranging approximately from 250 to 400 °C is attributed to Ni^0 oxidation that remained after catalytic tests, as the weight gain represents Ni oxidation, the gain was proportional to the Ni amount of the samples. The third region (III) ranging from 400 to 800 °C presents slight weight loss, representing carbon deposits oxidation [32,63]. Based on weight loss of region (III), carbon deposits were estimated as shown in Table 4. Although the carbon deposits after tests were low, the carbon amount increases when the M^{II}/M^{III} ratio decreases, which can be ascribed to the differences in the basic properties among the samples, as shown by the CO_2-TDP results. Low carbon deposition indicates that all samples have proper basic properties, which along with reactional parameters such as temperature range and H_2/CO_2 ratio were favorable to avoiding carbon formation [15,34].

Table 5 summarizes a comparison among the catalyst in this work and from literature, considering parameters where its maximum activity, selectivity, and stability were attained. Ni66Al33 stands out with higher CO_2 conversion and CH_4 selectivity despite presenting lower total basicity when compared to those from Wierzbicki et al. (2017) and Guo

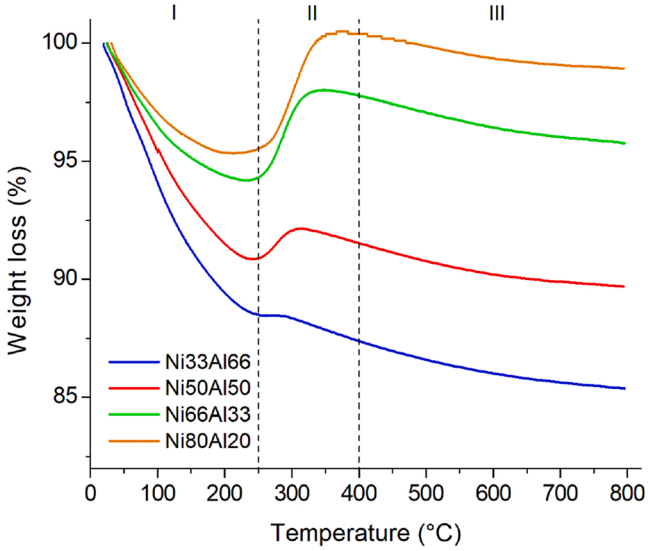

Fig. 10. TPO profiles of the spent Ni-Al catalysts after stability tests at 300 °C.

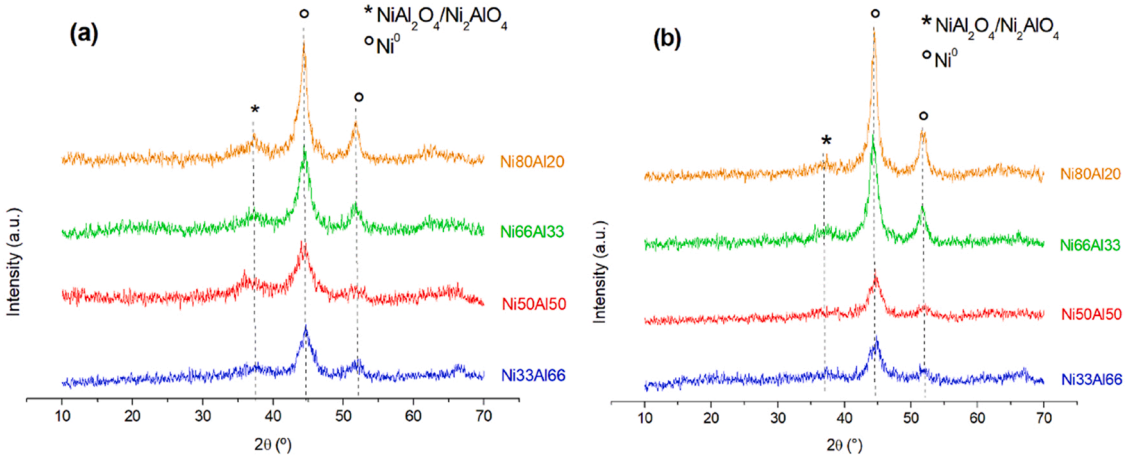

Fig. 9. XRD patterns of spent Ni-Al catalysts after (a) reactions between 200 and 400 °C, and (b) stability tests at 300 °C.

Table 5
Comparison of LDH-derived catalysts applied to CO_2 methanation.

Catalyst	Reactional parameters	XCO_2, SCH_4 at 300 °C (%)	CO_2 desorbed (μmol g_{cat}^{-1})	S^0_{Ni}, D^0_{Ni} (m^2 g_{cat}^{-1}, %)	D_{fresh} – D_{spent} (nm)	Reference
Ni66Al33	m_{cat} = 0.1 g, H_2/CO_2 = 4, P = 1 atm, T = 200–400 (300)[a] °C, GHSV = 60000 mL (g_{cat} h)$^{-1}$, 300 min[a]	92.3, 100	27.3	17.2, 3.2	2.8[b]/5.9[c]-4.3[d]/5.8[e]	This study
25Ni-Al_2O_3	m_{cat} = 0.2 g, H_2/CO_2 = 3.5, P = 1 atm, T = 200–500 (350)[a] °C, GHSV = 9000 mL (g_{cat} h)$^{-1}$, 600 min[a]	74, 100 (350 °C)	n/d	n/d	5.8[b]/6[c]	[28]
Ni-Al 12	m_{cat} = 0.6 (0.13)[a] g, H_2/CO_2 = 4, P = 1 (5)[a] bar T = 250–400 (300)[a] °C, GHSV = 20,000 h^{-1}, 1500 min[a]	85, 98	n/d	42.2, 13	3.6[b]	[27]
Ni42.5-Mg-Al	H_2/CO_2 = 4, P = 1 atm, T = 250–450 (250)[a] °C, GHSV = 12,000 h^{-1}, 1440 min[a]	82, 100	134	n/d	5[b]-5[d]	[31]
Ni_5Al-MO	m_{cat} = 0.5 g, H_2/CO_2 = 4, P = 1 atm, T = 150–400 (250)[a] °C, GHSV = 2400 h^{-1}, 7200 min[a]	89, 99 (250 °C)	1373	n/d	n/d	[30]
Ni-Al_2O_3-HT	m_{cat} = 0.04 g, H_2/CO_2 = 4, P = 1 atm, T = 200–400 (350)[a] °C, GHSV = 75,000 mL (g_{cat} h)$^{-1}$, 1200 min[a]	82.5, 99.4 (350 °C)	n/d	n/d	4[c]	[17]

[a] Reactional parameters of stability tests that differ from stepwise tests.
[b] for fresh calcined samples.
[c] for fresh reduced samples.
[d] for spent samples tested in stepwise mode.
[e] for spent samples tested in stability mode.

et al. (2018) [30,31]; less metallic surface area and dispersion than that of Abate et al. (2016) [27]; and variable reactional parameters such as lower sample mass and higher GHSV, except for that of He et al. (2014) [17]. All compared catalysts presented near 100 % CH_4 selectivity.

4. Conclusions

Ni-Al mixed oxides LDH-derived obtained by co-precipitation with variable M^{II}/M^{III} molar ratios were evaluated in CO_2 methanation. The increase in the M^{II}/M^{III} ratio caused a decrease in the specific surface area and a consequent increase in the crystallinity of the oxides. On the other hand, although the amount of H_2 consumed in the TPR increases with Ni content, i.e., with the M^{II}/M^{III} ratio, the amount of chemisorbed H_2 was higher for the sample with $M^{II}/M^{III} = 1$, while the greater number of alkaline sites were obtained for the sample with $M^{II}/M^{III} = 2$.

The catalysts were found to be highly active and selective towards CH_4 production, reaching 92.3 % CO_2 conversion and 100 % CH_4 selectivity at 300 °C for the sample with $M^{II}/M^{III} = 2$, attributed to their small crystallite size, improved metallic area, high dispersion, and high basicity, mainly in weak-to-medium strength range. The catalysts also presented high stability, maintaining their activity and selectivity during the time-on-stream tests, which is attributed to improved resistance to sintering, and low carbon formation. These results prove that LDH-derived Ni-Al catalysts with M^{II}/M^{III} molar ratios between 1 and 2 are highly suitable for CO_2 methanation.

CRediT authorship contribution statement

Yan Resing Dias: Investigation, Formal analysis, Writing – original draft. **Oscar W. Perez-Lopez:** Conceptualization, Supervision, Writing – review & editing.

Declaration of Competing Interest

The authors declare that they have no known competing financial interests or personal relationships that could have appeared to influence the work reported in this paper.

Data Availability

Data will be made available on request.

Acknowledgments

The authors acknowledge CNPq and CAPES through the PROEX Program for the financial support to carry out this work.

Appendix A. Supporting information

Supplementary data associated with this article can be found in the online version at doi:10.1016/j.jcou.2022.102381.

References

[1] D. Wierzbicki, M.V. Moreno, S. Ognier, M. Motak, T. Grzybek, P. Da Costa, M. E. Gálvez, Ni-Fe layered double hydroxide derived catalysts for non-plasma and DBD plasma-assisted CO_2 methanation, Int. J. Hydrogen Energy (2019) 2–11, https://doi.org/10.1016/j.ijhydene.2019.06.095.
[2] M.A.A. Aziz, A.A. Jalil, S. Triwahyono, M.W.A. Saad, CO_2 methanation over Ni-promoted mesostructured silica nanoparticles: influence of Ni loading and water vapor on activity and response surface methodology studies, Chem. Eng. J. 260 (2015) 757–764, https://doi.org/10.1016/j.cej.2014.09.031.
[3] B. Petroleum, Statistical Review of World Energy globally consistent data on world energy markets and authoritative publications in the field of energy, BP Energy Outlook 2021. 70 (2021) 8–20.
[4] L. Yin, X. Chen, M. Sun, B. Zhao, J. Chen, Q. Zhang, P. Ning, Insight into the role of Fe on catalytic performance over the hydrotalcite-derived Ni-based catalysts for CO_2 methanation reaction, Int. J. Hydrogen Energy 47 (2022) 7139–7149, https://doi.org/10.1016/j.ijhydene.2021.12.057.
[5] K. Sawahara, K. Yatagai, T. Boll, A. Pundt, R. Gemma, Role of atomic hydrogen supply on the onset of CO_2 methanation over La–Ni based hydrogen storage alloys studied by in-situ approach, Int. J. Hydrogen Energy 47 (2022) 19051–19061, https://doi.org/10.1016/j.ijhydene.2022.04.089.
[6] S. Meesattham, P. Kim-Lohsoontorn, Low-temperature alcohol-assisted methanol synthesis from CO_2 and H_2: The effect of alcohol type, Int. J. Hydrogen Energy 47 (2022) 22691–22703, https://doi.org/10.1016/j.ijhydene.2022.05.083.
[7] B.M. Al–Swai, N.B. Osman, A. Ramli, B. Abdullah, A.S. Farooqi, B.V. Ayodele, D. O. Patrick, Low-temperature catalytic conversion of greenhouse gases (CO_2 and CH_4) to syngas over ceria-magnesia mixed oxide supported nickel catalysts, Int. J. Hydrogen Energy 46 (2021) 24768–24780, https://doi.org/10.1016/j.ijhydene.2020.04.233.
[8] S. Walspurger, G.D. Elzinga, J.W. Dijkstra, M. Sarić, W.G. Haije, Sorption enhanced methanation for substitute natural gas production: experimental results and thermodynamic considerations, Chem. Eng. J. 242 (2014) 379–386, https://doi.org/10.1016/j.cej.2013.12.045.
[9] E. Giglio, A. Lanzini, M. Santarelli, P. Leone, Synthetic natural gas via integrated high-temperature electrolysis and methanation: Part I-Energy performance, J. Energy Storage 1 (2015) 22–37, https://doi.org/10.1016/j.est.2015.04.002.
[10] A. Banu, Y. Bicer, Integration of methane cracking and direct carbon fuel cell with CO_2 capture for hydrogen carrier production, Int. J. Hydrogen Energy 47 (2022) 19502–19516, https://doi.org/10.1016/j.ijhydene.2022.04.187.
[11] C. Lv, L. Xu, M. Chen, Y. Cui, X. Wen, Y. Li, C.E. Wu, B. Yang, Z. Miao, X. Hu, Q. Shou, Recent progresses in constructing the highly efficient Ni based catalysts with advanced low-temperature activity toward CO_2 methanation, Front. Chem. 8 (2020) 1–32, https://doi.org/10.3389/fchem.2020.00269.
[12] P. Shafiee, S.M. Alavi, M. Rezaei, Mechanochemical synthesis method for the preparation of mesoporous Ni–Al2O3 catalysts for hydrogen purification via CO_2

methanation, J. Energy Inst. 96 (2021) 1–10, https://doi.org/10.1016/j.joei.2021.01.015.
[13] S. Valinejad Moghaddam, M. Rezaei, F. Meshkani, R. Daroughegi, Carbon dioxide methanation over Ni-M/Al_2O_3 (M: Fe, Co, Zr, La and Cu) catalysts synthesized using the one-pot sol-gel synthesis method, Int. J. Hydrogen Energy 43 (2018) 16522–16533, https://doi.org/10.1016/j.ijhydene.2018.07.013.
[14] K. Stangeland, D. Kalai, H. Li, Z. Yu, CO_2 methanation: the effect of catalysts and reaction conditions, Energy Procedia 105 (2017) 2022–2027, https://doi.org/10.1016/j.egypro.2017.03.577.
[15] C. Mebrahtu, F. Krebs, S. Abate, S. Perathoner, G. Centi, R. Palkovits, CO_2 Methanation: Principles and Challenges, 1st ed., Elsevier B.V, 2019 https://doi.org/10.1016/B978-0-444-64127-4.00005-7.
[16] J. Gao, Y. Wang, Y. Ping, D. Hu, G. Xu, F. Gu, F. Su, A thermodynamic analysis of methanation reactions of carbon oxides for the production of synthetic natural gas, RSC Adv. 2 (2012) 2358–2368, https://doi.org/10.1039/c2ra00632d.
[17] L. He, Q. Lin, Y. Liu, Y. Huang, Unique catalysis of Ni-Al hydrotalcite derived catalyst in CO_2 methanation: cooperative effect between Ni nanoparticles and a basic support, J. Energy Chem. 23 (2014) 587–592, https://doi.org/10.1016/S2095-4956(14)60144-3.
[18] W.J. Lee, C. Li, H. Prajitno, J. Yoo, J. Patel, Y. Yang, S. Lim, Recent trend in thermal catalytic low temperature CO_2 methanation: a critical review, Catal. Today 368 (2021) 2–19, https://doi.org/10.1016/j.cattod.2020.02.017.
[19] Z. Liu, X. Gao, B. Liu, Q. Ma, T. sheng Zhao, J. Zhang, Recent advances in thermal catalytic CO_2 methanation on hydrotalcite-derived catalysts, Fuel 321 (2022), 124115, https://doi.org/10.1016/j.fuel.2022.124115.
[20] H. Lu, X. Yang, G. Gao, J. Wang, C. Han, X. Liang, C. Li, Y. Li, W. Zhang, X. Chen, Metal (Fe, Co, Ce or La) doped nickel catalyst supported on ZrO 2 modified mesoporous clays for CO and CO_2 methanation, Fuel 183 (2016) 335–344, https://doi.org/10.1016/j.fuel.2016.06.084.
[21] J. Kirchner, J.K. Anolleck, H. Lösch, S. Kureti, Methanation of CO_2 on iron based catalysts, Appl. Catal. B Environ. 223 (2018) 47–59, https://doi.org/10.1016/j.apcatb.2017.06.025.
[22] M.A.A. Aziz, A.A. Jalil, S. Triwahyono, R.R. Mukti, Y.H. Taufiq-Yap, M.R. Sazegar, Highly active Ni-promoted mesostructured silica nanoparticles for CO_2 methanation, Appl. Catal. B Environ. 147 (2014) 359–368, https://doi.org/10.1016/j.apcatb.2013.09.015.
[23] C. Liang, H. Tian, G. Gao, S. Zhang, Q. Liu, D. Dong, X. Hu, Methanation of CO_2 over alumina supported nickel or cobalt catalysts: effects of the coordination between metal and support on formation of the reaction intermediates, Int. J. Hydrogen Energy 45 (2020) 531–543, https://doi.org/10.1016/j.ijhydene.2019.10.195.
[24] X. Fang, C. Chen, H. Jia, Y. Li, J. Liu, Y. Wang, Y. Song, T. Du, L. Liu, Progress in adsorption-enhanced hydrogenation of CO_2 on layered double hydroxide (LDH) derived catalysts, J. Ind. Eng. Chem. 95 (2021) 16–27, https://doi.org/10.1016/j.jiec.2020.12.027.
[25] R. Daroughegi, F. Meshkani, M. Rezaei, Characterization and evaluation of mesoporous high surface area promoted Ni-Al_2O_3 catalysts in CO_2 methanation, J. Energy Inst. 93 (2020) 482–495, https://doi.org/10.1016/j.joei.2019.07.003.
[26] D. Wierzbicki, M. Motak, T. Grzybek, M.E. Gálvez, P. Da Costa, The influence of lanthanum incorporation method on the performance of nickel-containing hydrotalcite-derived catalysts in CO_2 methanation reaction, Catal. Today 307 (2018) 205–211, https://doi.org/10.1016/j.cattod.2017.04.020.
[27] S. Abate, K. Barbera, E. Giglio, F. Deorsola, S. Bensaid, S. Perathoner, R. Pirone, G. Centi, Synthesis, characterization, and activity pattern of Ni-Al hydrotalcite catalysts in CO_2 methanation, Ind. Eng. Chem. Res. 55 (2016) 8299–8308, https://doi.org/10.1021/acs.iecr.6b01581.
[28] R. Daroughegi, F. Meshkani, M. Rezaei, Enhanced activity of CO_2 methanation over mesoporous nanocrystalline Ni–Al_2O_3 catalysts prepared by ultrasound-assisted co-precipitation method, Int. J. Hydrogen Energy 42 (2017) 15115–15125, https://doi.org/10.1016/j.ijhydene.2017.04.244.
[29] M. Gabrovska, R. Edreva-Kardjieva, D. Crişan, P. Tzvetkov, M. Shopska, I. Shtereva, Ni-Al layered double hydroxides as catalyst precursors for CO_2 removal by methanation, React. Kinet. Mech. Catal. 105 (2012) 79–99, https://doi.org/10.1007/s11144-011-0378-0.
[30] X. Guo, Z. Peng, M. Hu, C. Zuo, A. Traitangwong, V. Meeyoo, C. Li, S. Zhang, Highly active Ni-based catalyst derived from double hydroxides precursor for low temperature CO_2 methanation, Ind. Eng. Chem. Res. 57 (2018) 9102–9111, https://doi.org/10.1021/acs.iecr.8b01619.
[31] D. Wierzbicki, R. Baran, R. Dębek, M. Motak, T. Grzybek, M.E. Gálvez, P. Da Costa, The influence of nickel content on the performance of hydrotalcite-derived catalysts in CO_2 methanation reaction, Int. J. Hydrogen Energy 42 (2017) 23548–23555, https://doi.org/10.1016/j.ijhydene.2017.02.148.
[32] D. dos, S. Lima, Y.R. Dias, O.W. Perez-Lopez, CO_2 methanation over Ni-Al and Co-Al LDH-derived catalysts: the role of basicity, Sustain. Energy Fuels 4 (2020) 5747–5756, https://doi.org/10.1039/d0se01059f.
[33] C.O. Calgaro, O.W. Perez-Lopez, Biogas dry reforming for hydrogen production over Ni-M-Al catalysts (M = Mg, Li, Ca, La, Cu, Co, Zn), Int. J. Hydrogen Energy 44 (2019) 17750–17766, https://doi.org/10.1016/j.ijhydene.2019.05.113.
[34] M. Rosset, L.A. Féris, O.W. Perez-Lopez, Biogas dry reforming using Ni–Al-LDH catalysts reconstructed with Mg and Zn, Int. J. Hydrogen Energy 46 (2021) 20359–20376, https://doi.org/10.1016/j.ijhydene.2021.03.150.
[35] L.G.T. Gouveia, C.B. Agustini, O.W. Perez-Lopez, M. Gutterres, CO_2 adsorption using solids with different surface and acid-base properties, J. Environ. Chem. Eng. 8 (2020), 103823, https://doi.org/10.1016/j.jece.2020.103823.
[36] S. Li, G. Liu, S. Zhang, K. An, Z. Ma, L. Wang, Y. Liu, Cerium-modified Ni-La_2O_3/ZrO_2 for CO_2 methanation, J. Energy Chem. 43 (2020) 155–164, https://doi.org/10.1016/j.jechem.2019.08.024.
[37] K. Stangeland, D.Y. Kalai, H. Li, Z. Yu, Active and stable Ni based catalysts and processes for biogas upgrading: the effect of temperature and initial methane concentration on CO_2 methanation, Appl. Energy 227 (2018) 206–212, https://doi.org/10.1016/j.apenergy.2017.08.080.
[38] F.G. Denardin, O.W. Perez-Lopez, Methane dehydroaromatization over Fe-M/ZSM-5 catalysts (M= Zr, Nb, Mo), Microporous Mesoporous Mater. 295 (2020), 109961, https://doi.org/10.1016/j.micromeso.2019.109961.
[39] Y.R. Dias, O.W. Perez-Lopez, Effect of Ni/Cu ratio on activity and selectivity of CO_2 methanation over Ni-Cu/SiO_2 catalysts, Greenh. Gases Sci. Technol. 12 (2022) 156–169, https://doi.org/10.1002/ghg.2133.
[40] Y.R. Dias, O.W. Perez-Lopez, CO_2 conversion to methane using Ni/SiO_2 catalysts promoted by Fe, Co and Zn, J. Environ. Chem. Eng. 9 (2021), 104629, https://doi.org/10.1016/j.jece.2020.104629.
[41] D.S. Lima, O.W. Perez-Lopez, Synthesis and properties of template-free mesoporous alumina and its application in gas phase dehydration of glycerol, Powder Technol. 378 (2021) 737–745, https://doi.org/10.1016/j.powtec.2020.10.031.
[42] K. Wu, Q. Ye, L. Wang, F. Meng, H. Dai, Mesoporous alumina-supported layered double hydroxides for efficient CO_2 capture, J. CO_2 Util. 60 (2022), 101982, https://doi.org/10.1016/j.jcou.2022.101982.
[43] M. Thommes, K. Kaneko, A.V. Neimark, J.P. Olivier, F. Rodriguez-Reinoso, J. Rouquerol, K.S.W. Sing, Physisorption of gases, with special reference to the evaluation of surface area and pore size distribution (IUPAC Technical Report), Pure Appl. Chem. 87 (2015) 1051–1069, https://doi.org/10.1515/pac-2014-1117.
[44] T. Burger, F. Koschany, O. Thomys, K. Köhler, O. Hinrichsen, CO_2 methanation over Fe- and Mn-promoted co-precipitated Ni-Al catalysts: Synthesis, characterization and catalysis study, Appl. Catal. A Gen. 558 (2018) 44–54, https://doi.org/10.1016/j.apcata.2018.03.021.
[45] M. Wolf, L.H. Wong, C. Schüler, O. Hinrichsen, CO_2 methanation on transition-metal-promoted Ni-Al catalysts: sulfur poisoning and the role of CO_2 adsorption capacity for catalyst activity, J. CO_2 Util. 36 (2020) 276–287, https://doi.org/10.1016/j.jcou.2019.10.014.
[46] W.O. Alabi, CO_2 reforming of CH_4 on Ni-Al-O_x catalyst using pure and coal gas feeds: synergetic effect of CoO and MgO in mitigating carbon deposition, Environ. Pollut. 242 (2018) 1566–1576, https://doi.org/10.1016/j.envpol.2018.07.127.
[47] L. Zhang, L. Bian, Z. Zhu, Z. Li, La-promoted Ni/Mg-Al catalysts with highly enhanced low-temperature CO_2 methanation performance, Int. J. Hydrogen Energy 43 (2018) 2197–2206, https://doi.org/10.1016/j.ijhydene.2017.12.082.
[48] S. Ewald, M. Kolbeck, T. Kratky, M. Wolf, O. Hinrichsen, On the deactivation of Ni-Al catalysts in CO_2 methanation, Appl. Catal. A Gen. 570 (2019) 376–386, https://doi.org/10.1016/j.apcata.2018.10.033.
[49] Z. Zhang, T. Wei, G. Chen, C. Li, D. Dong, W. Wu, Q. Liu, X. Hu, Understanding correlation of the interaction between nickel and alumina with the catalytic behaviors in steam reforming and methanation, Fuel 250 (2019) 176–193, https://doi.org/10.1016/j.fuel.2019.04.005.
[50] D. Wierzbicki, R. Debek, M. Motak, T. Grzybek, M.E. Gálvez, P. Da Costa, Novel Ni-La-hydrotalcite derived catalysts for CO_2 methanation, Catal. Commun. 83 (2016) 5–8, https://doi.org/10.1016/j.catcom.2016.04.021.
[51] Q. Pan, J. Peng, T. Sun, S. Wang, S. Wang, Insight into the reaction route of CO_2 methanation: Promotion effect of medium basic sites, Catal. Commun. 45 (2014) 74–78, https://doi.org/10.1016/j.catcom.2013.10.034.
[52] M.A.A. Aziz, A.A. Jalil, S. Wongsakulphasatch, D.V.N. Vo, Understanding the role of surface basic sites of catalysts in CO_2 activation in dry reforming of methane: a short review, Catal. Sci. Technol. 10 (2020) 35–45, https://doi.org/10.1039/c9cy01519a.
[53] Y. Zhao, S. Zhao, Y. Geng, Y. Shen, H. Yue, J. Lv, S. Wang, X. Ma, Ni-containing Cu/SiO_2 catalyst for the chemoselective synthesis of ethanol via hydrogenation of dimethyl oxalate, Catal. Today 276 (2016) 28–35, https://doi.org/10.1016/j.cattod.2016.01.053.
[54] W. Karim, C. Spreafico, A. Kleibert, J. Gobrecht, J. Vandevondele, Y. Ekinci, J.A. Van Bokhoven, Catalyst support effects on hydrogen spillover, Nature 541 (2017) 68–71, https://doi.org/10.1038/nature20782.
[55] H. Shen, H. Li, Z. Yang, C. Li, Magic of hydrogen spillover: Understanding and application, Green Energy Environ. (2022), https://doi.org/10.1016/j.gee.2022.01.013.
[56] D.C.D. Da Silva, S. Letichevsky, L.E.P. Borges, L.G. Appel, The Ni/ZrO_2 catalyst and the methanation of CO and CO_2, Int. J. Hydrogen Energy 37 (2012) 8923–8928, https://doi.org/10.1016/j.ijhydene.2012.03.020.
[57] A.G. Boudjahem, M. Pietrowski, S. Monteverdi, M. Mercy, M.M. Bettahar, Structural and surface propperties of Ni-Cu nanoparticles supported on SiO2, J. Mater. Sci. 41 (2006) 2025–2030, https://doi.org/10.1007/s10853-006-2150-9.
[58] T. Schaaf, J. Grünig, M.R. Schuster, T. Rothenfluh, A. Orth, Methanation of CO_2 - storage of renewable energy in a gas distribution system, Energy Sustain. Soc. 4 (2014) 1–14, https://doi.org/10.1186/s13705-014-0029-1.
[59] J. Gao, Y. Wang, Y. Ping, D. Hu, G. Xu, F. Gu, F. Su, A thermodynamic analysis of methanation reactions of carbon oxides for the production of synthetic natural gas, RSC Adv. 2 (2012) 2358–2368, https://doi.org/10.1039/c2ra00632d.
[60] S.V. Moghaddam, M. Rezaei, F. Meshkani, R. Daroughegi, Synthesis of nanocrystalline mesoporous Ni/Al_2O_3–SiO_2 catalysts for CO_2 methanation reaction, Int. J. Hydrogen Energy 43 (2018) 19038–19046, https://doi.org/10.1016/j.ijhydene.2018.08.163.
[61] W.K. Fan, M. Tahir, Recent trends in developments of active metals and heterogenous materials for catalytic CO_2 hydrogenation to renewable methane: a

review, J. Environ. Chem. Eng. 9 (2021), 105460, https://doi.org/10.1016/j.jece.2021.105460.

[62] T.A. Le, J. Kim, J.K. Kang, E.D. Park, CO and CO_2 methanation over M (M = Mn, Ce, Zr, Mg, K, Zn, or V)-promoted Ni/Al@Al2O3 catalysts, Catal. Today (2019) 1–9, https://doi.org/10.1016/j.cattod.2019.08.058.

[63] Y.R. Dias, O.W. Perez-Lopez, Carbon dioxide methanation over Ni-Cu/SiO_2 catalysts, Energy Convers. Manag. 203 (2020), 112214, https://doi.org/10.1016/j.enconman.2019.112214.

[64] O.W. Perez-Lopez, A. Senger, N.R. Marcilio, M.A. Lansarin, Effect of composition and thermal pretreatment on properties of Ni−Mg−Al catalysts for CO_2 reforming of methane, Appl. Catal. A Gen. 303 (2006) 234–244, https://doi.org/10.1016/j.apcata.2006.02.024.

[65] L. Zardin, O.W. Perez-Lopez, Hydrogen production by methane decomposition over Co-Al mixed oxides derived from hydrotalcites: effect of the catalyst activation with H2 or CH4, Int. J. Hydrogen Energy 42 (2017) 7895–7907, https://doi.org/10.1016/j.ijhydene.2017.02.153.